A three-dimensional model for T-shaped acoustic resonators with sound absorption materials

Ganghua Yu, Li Cheng,[a] and Deyu Li
Department of Mechanical Engineering, The Hong Kong Polytechnic University, Hung Hom, Kowloon, Hong Kong, China

(Received 11 September 2010; revised 25 January 2011; accepted 10 February 2011)

Recent development in noise control using T-shaped acoustic resonators calls for the development of more reliable and accurate models to predict their acoustic characteristics, which is unfortunately lacking in the literature. This paper attempts to establish such a model based on three-dimensional theory for T-shaped acoustic resonators containing sound absorption materials. The model is validated by experiments using various configurations. Predictions on fundamental and high-order resonance frequencies are compared with those obtained from the one-dimensional model and finite element analyses, and the effects of the physical and geometric parameters of the absorption materials on the resonance frequencies and Q-factor are also investigated numerically and experimentally. Limitations and applicability of existing one-dimensional models are assessed. The proposed general three-dimensional model proved to be able to provide an accurate and reliable prediction on the resonance frequencies for T-shaped acoustic resonators with or without absorption materials. This can eventually meet the requirement for resonator array design in terms of accuracy.
 [DOI: 10.1121/1.3560917]

PACS number(s): 43.50.Gf, 43.20.Mv [FCS] Pages: 3000–3010

I. INTRODUCTION

Research on low-frequency noise control using acoustic resonators has been revitalized due to a number of recent developments in terms of resonator design, system optimization, and implementation. Among these efforts, the T-shaped acoustic resonators (TARs) show great potential in controlling noise inside acoustic cavities.[1–3] Owing to the large aspect ratio, a TAR can be embedded into the walls or structures enclosing the cavity to form a compact system by minimizing the space required by installation. Upon proper design, multiple TARs can be used to form a resonator array for achieving a broad band sound reduction.[4,5]

A typical TAR consists of two mutually perpendicular tubes: a long closed-end tube and a short open-end one. A theoretical model was first proposed by Merkli based on one-dimensional (1-D) pipe assumption,[6] in which the TAR was divided into three branches and a common junction shared by these branches. Two assumptions were made in the modeling process: (a) only plane wave propagating in all branches and (b) a uniform pressure distributing in the common junction. The derived model required end corrections which depended on the lengths of the branches. Meanwhile, the study is rather restrictive in that the model was limited to TARs that only had the same circular cross-section for all branches with equal lengths for the two coaxial branches. In a later study on the TAR, Li and Vipperman extended Merkli's model to more general configurations under the same 1-D assumption.[7] Different methods in determining the internal end corrections for all branches were developed. Among them, the empirical Hybrid Rayleigh's end corrections, depending only on the radius of branches, gave the best predictions. Li and Vipperman's 1-D model is simple enough, which was used to guide the TAR design in engineering applications with some success.[2–5] Similar T-junction tubes were also investigated by Dubos *et al.*[8] They developed a 1-D model to describe the discontinuity at the junction. The radiation impedance at the orifice of TARs was calculated as the added acoustic mass, which was derived on the basis of the multiple-modal method.

In the design of TARs, the lengths of some branches are expected to be short, which may be comparable to or even smaller than their transverse dimensions. Therefore, the commonly adopted 1-D plane wave assumption[9–11] becomes quite debatable and produces unacceptable errors. Although the empirical end corrections can compensate for the error of that simplification to certain extent for a limited number of configurations,[7] more general cases cannot be handled. Meanwhile, apart from the cross-sectional areas and the tube lengths, other geometrical parameters such as the ratio between the cross-sectional width and height in the case where the tube is rectangular are not considered in the above two 1-D models.

Multiple-dimensional models have been developed to accurately predict the fundamental resonance frequency for the conventional Helmholtz resonators (HRs).[11–13] However, these models cannot be used for TARs because of the obvious difference in geometry between the HRs and TARs.

In a previous attempt to control the interior sound pressure inside a cavity, it was observed that an accurate prediction and meticulous tuning of the Helmholtz frequencies are crucial to ensure an effective control.[3–5] This becomes even more critical when multiple resonators are needed to enlarge the control band. Errors produced by existing 1-D models can easily be large enough to jeopardize the performance of

[a]Author to whom correspondence should be addressed. Electronic mail: mmlcheng@polyu.edu.hk

 0001-4966/2011/129(5)/3000/11/$30.00

the resonator array. It was shown that, depending on the targeted bandwidth, fine tuning of the Helmholtz frequencies[3–5] and damping[14] of resonators allowed a compromised balance between the reaction effect and dissipation effect of the resonators to achieve an optimized control performance. Damping of resonators is usually tuned by inserting sound absorption materials, which existing 1-D models cannot accommodate. All these show a real need for a general and accurate 3-D TAR model, which can be incorporated into the resonator optimization procedure.[4]

Therefore, this paper aims to develop an accurate three-dimensional (3-D) model for the TAR to design its geometric dimensions and to predict its physical parameters. Since high frequency noise can be readily handled by many existing means such as damping and dissipation, the scope of application for acoustic resonators is the low-frequency range. Therefore, the targeted frequency range of this model is also the low-frequency range. Instead of exploring proper internal end corrections used in 1-D model, the propagation of 3-D wave inside TAR is analyzed. The effect of absorption material inside a TAR on its resonance frequencies is investigated. The predicted resonance frequencies are compared with numerical simulations obtained from the 1-D model and the finite element method (FEM). Experiments are also conducted to validate the 3-D model.

II. THEORY

In the current work, the tubes of the TAR have square shape as shown in Fig. 1. The short one is referred to as tube 1, having the physical length L_1 and cross-sectional dimensions $h_1 \times b_1$. The longer one is called tube 2 whose cross-section dimensions are $h_2 \times b_2$ and physical length is $L_2 + L_3 + h_1$. In the present model, tube 2 is modeled as a whole, instead of being divided into three parts like in the 1-D model. All surrounding walls of the TAR are assumed to be rigid. Throughout the paper, the superscripts T1 and T2 indicate tubes 1 and 2, respectively. In this section, the sound field inside tubes 1 and 2 are analyzed with/without absorption materials, and the input acoustic impedance of the TAR at the aperture is derived to calculate the resonance frequency.

The pressure field in the TAR is governed by the wave equation[15]

$$\nabla^2 p(\mathbf{r},t) - \frac{1}{c^2}\ddot{p}(\mathbf{r},t) = -\rho_0 \dot{q}(t)\delta(\mathbf{r}-\mathbf{r}_0), \quad (1)$$

where $p(\mathbf{r}, t)$ is the acoustic pressure; $q(t)$ is the volume velocity of the source at $\mathbf{r}_0$; c is the sound speed; ρ_0 is the air density; and $\delta(\mathbf{r}-\mathbf{r}_0)$ is the 3-D Dirac delta function. Assuming the source volume velocity is harmonic, i.e., $q(t) = Q_0 e^{i\omega t}$, the solution of Eq. (1) can be written as $p(\mathbf{r}, t) = P(\mathbf{r})e^{i\omega t}$. For convenience, the harmonic item $e^{i\omega t}$ will be omitted in the following discussion.

A. Sound field in tube 1

The sound pressure can be further decomposed on the basis of cross-sectional duct-modes. Therefore, the solution of sound pressure in tube 1 can be expressed as

$$P^{T1}(x,y,z) = \sum_{q,r} \phi_{qr}(x,z)\left[A_{qr}^{+} e^{-iK_{qr}^{T1} y} + A_{qr}^{-} e^{iK_{qr}^{T1} y}\right], \quad (2)$$

where $\phi_{qr}(x, z)$ are the cross-sectional mode shape functions of tube 1, in which q and r are the indices of cross-sectional acoustic modes along x and z directions, respectively; ω is the angular frequency; A_{qr}^{+} and A_{qr}^{-} are the unknown coefficients; K_{qr}^{T1} is the propagation constant along the axis of tube 1 given by $-i\sqrt{(\kappa_{qr}^{T1})^2 - \tilde{k}_1^2}$, where κ_{qr}^{T1} is the cross-sectional characteristic propagation constant computed by $(\kappa_{qr}^{T1})^2 = (2q\pi/h_1)^2 + (2r\pi/b_1)^2$ and $\tilde{k}_1$ is the complex propagation constant. $\tilde{k}_1$ can be approximately expressed with a dispersion relation $\tilde{k}_1 = k - i\alpha_w$, in which k is the propagation constant without absorption given by ω/c and α_w is the absorption coefficient of tubes defined in Ref. 16.

The modal shape functions $\phi(x, z)$ have the orthogonality properties as

$$\frac{1}{S^{T1}}\iint_{S^{T1}} \phi_{qr}(x,z)\phi_{\mu\nu}^{*}(x,z)dxdz = \begin{cases} 0, & \mu,\nu \neq q,r \\ 1 & \mu,\nu = q,r \end{cases},$$

where S^{T1} is the cross-sectional area of tube 1.

For the hard-walled tube, the normalized mode shape function for the rectangular cross-section is[17]

$$\phi_{qr}(x,z) = \sqrt{(2-\delta_{0q})(2-\delta_{0r})}\cos\frac{2q\pi x}{h_1}\cos\frac{2r\pi z}{b_1},$$

where $\delta_{\mu\nu}$ is the Kronecker delta function, which is equal to zero when $\mu \neq \nu$ and unity when $\mu = \nu$. Under the harmonic assumption, the yth component of the particle velocity u_y^{T1} is computed using the linear Euler's equation as

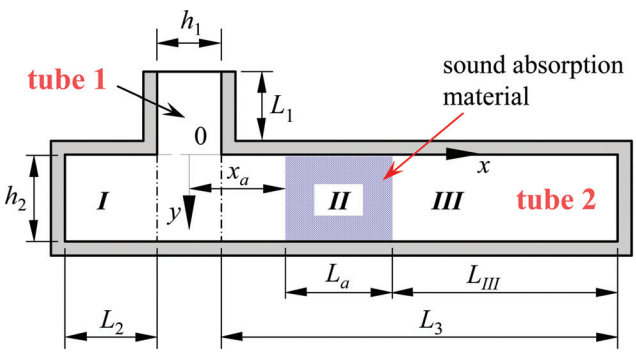

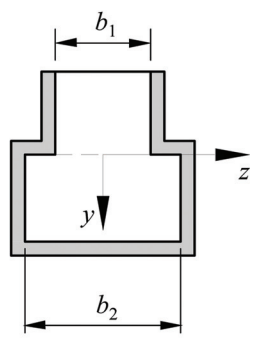

FIG. 1. (Color online) TARs with absorption material.

$$u_y^{T1} = -\frac{1}{i\omega\rho_0}\frac{\partial P}{\partial y}. \tag{3}$$

Substituting Eq. (2) into Eq. (3), u_y^{T1} is given by

$$u_y^{T1} = -\frac{1}{i\omega\rho_0}\sum_{q,r}\phi_{qr}(x,z)\left[-iK_{qr}^{T1}A_{qr}^{+}e^{-iK_{qr}^{T1}y} + iK_{qr}^{T1}A_{qr}^{-}e^{iK_{qr}^{T1}y}\right]. \tag{4}$$

In the present study, the velocity distribution over the orifice is assumed to be uniform and has amplitude U_s. The corresponding velocity boundary condition requires

$$u_y^{T1}\Big|_{y=-L_{\text{eff}}^{T1}} = U_S, |x| \le \frac{h_1}{2}, |z| \le \frac{b_1}{2}, \tag{5}$$

where L_{eff}^{T1} is the effective length of tube 1 by adding its physical length L_1 and the external end correction ΔL. Considering that acoustic resonators are usually used to control low-frequency noise, i.e., kb_1 $(kh_1) \ll 1$, ΔL can be approximately calculated by $\Delta L = 8(b_1^2 + b_1h_1 + h_1^2)/9\pi(b_1 + h_1)$.[18]

Substituting Eq. (4) into Eq. (5) and utilizing the orthogonal properties of mode shapes yield

$$A_{\mu\nu}^{+}e^{iK_{\mu\nu}^{T1}L_{\text{eff}}^{T1}} - A_{\mu\nu}^{-}e^{-iK_{\mu\nu}^{T1}L_{\text{eff}}^{T1}} = \frac{\omega\rho_0}{S^{T1}K_{\mu\nu}^{T1}}\iint_{S^{T1}} U_S\phi_{\mu\nu}(x,z)dS.$$

For $\mu = 0$ and $\nu = 0$,

$$A_0^{+}e^{iK_0^{T1}L_{\text{eff}}^{T1}} - A_0^{-}e^{-iK_0^{T1}L_{\text{eff}}^{T1}} = \frac{\omega\rho_0}{K_0^{T1}}U_S \tag{6}$$

and for $\mu \neq 0$ or $\nu \neq 0$,

$$A_{\mu\nu}^{+}e^{iK_{\mu\nu}^{T1}L_{\text{eff}}^{T1}} - A_{\mu\nu}^{-}e^{-iK_{\mu\nu}^{T1}L_{\text{eff}}^{T1}} = 0. \tag{7}$$

At the end $y = 0$, u_y^{T1} reduces to

$$u_0^{T1} = \frac{1}{\omega\rho_0}\sum_{q,r}K_{qr}^{T1}\phi_{qr}(x,z)\left[A_{qr}^{+} - A_{qr}^{-}\right]. \tag{8}$$

This velocity distribution can be treated as the sound source creating the sound field in tube 2. It will be used to calculate the pressure field in the tube 2 in Sec. II B.

B. Sound field in tube 2

The sound field inside tube 2, containing sound absorption materials, is first examined. Then, the model without absorption materials can be simplified from the derived equations. Let absorption materials be installed inside the tube 2 at $x = x_a$ $(x_a \ge h_1/2)$ with a length L_a (Segment II), as shown in Fig. 1. The two segments divided by the absorption materials are referred to as segments I and III, respectively. The pressure field in the segment I can be separated into two parts: the sound radiated from the velocity distribution u_0^{T1}, and the sound induced by all boundaries of the tube 2. According to Doak's work, the radiated sound pressure by a sound source distribution in an infinite rigid-walled duct can be expressed as[19]

$$P_{\text{rad}}^{T2}(x,y,z) = \rho_0\sum_{m,n}\frac{\omega\psi_{mn}(y,z)}{2S^{T2}K_{mn}^{T2}}\iint_{S^{T1}}\left[H(x-x')e^{-iK_{mn}^{T2}(x-x')} + H(x'-x)e^{iK_{mn}^{T2}(x-x')}\right]\psi_{mn}^{*}(0,z')u_0^{T1}dS', \tag{9}$$

where S^{T2} is the cross-sectional area of tube 2 ψ_{mn} are the cross-sectional mode shape functions in tube 2, in which m and n are the indices of cross-sectional acoustic modes along y and z directions, respectively; H is the Heaviside function; K_{mn}^{T2} is the propagation constant along the axis of tube 2 given by $-i\sqrt{(\kappa_{mn}^{T2})^2 - \tilde{k}_2^2}$, in which κ_{mn}^{T2} is the cross-sectional characteristic propagation constant computed by $(\kappa_{mn}^{T2})^2 = (2m\pi/h_2)^2 + (2n\pi/b_2)^2$ and $\tilde{k}_2$ is the complex acoustic propagation constant given by $\tilde{k}_2 = k - i\alpha_w$; and x' is the source location. This equation is the convolution product of the Green function and the source distribution, where the Green function is the solution of the acoustic field excited by a harmonic point source in an infinite rigid-walled duct.[19]

The acoustic mode shape functions of tube 2 are also orthogonal to each other, having

$$\frac{1}{S^{T2}}\iint_{S^{T2}}\psi_{mn}(y,z)\psi_{\mu\nu}^{*}(y,z)dydz = \begin{cases} 0, & \mu,\nu \neq m,n \\ 1, & \mu,\nu = m,n \end{cases},$$

The normalized $\psi_{mn}(y, z)$ for rigid-walled duct takes the form

$$\psi_{mn}(y,z) = \sqrt{(2-\delta_{0m})(2-\delta_{0n})}\cos\frac{m\pi y}{h_2}\cos\frac{2n\pi z}{b_2}.$$

Using the construction of the radiation pressure in Eq. (9), the sound in segment I induced by the boundaries can be expressed as[20]

$$P_{\text{ref}}^{T2}(x,y,z) = \rho_0\sum_{m,n}\frac{\omega\psi_{mn}(y,z)}{2S^{T2}K_{mn}^{T2}}\iint_{S^{T1}}\left[B_{mn}^{+}e^{-iK_{mn}^{T2}(x-x')} + B_{mn}^{-}e^{iK_{mn}^{T2}(x-x')}\right]\psi_{mn}^{*}(0,z')u_0^{T1}dS', \tag{10}$$

where B_{mn}^{+} and B_{mn}^{-} are the unknown coefficients. Equation (10) actually not only describes the reflections at the two ends of segment I but also involves the effect of other interfaces in tube 2 since this segment communicates with other two segments. It is noted that Eq. (10) automatically satisfies the boundary condition at the interface between two tubes.

Similarly, the pressure response in segment II can be also decomposed on the basis of duct-modes as

$$P_{\text{abs}}^{T2}(x,y,z) = \sum_{m,n}\psi_{mn}(y,z)\left[C_{mn}^{+}e^{-i\tilde{K}_{mn}^{T2}(x-x_a)} + C_{mn}^{-}e^{i\tilde{K}_{mn}^{T2}(x-x_a)}\right], \tag{11}$$

where $\tilde{K}_{mn}^{T2}$ is the propagation constant along the axis of tube 2 computed by $-i\sqrt{(\kappa_{mn}^{T2})^2 - \tilde{k}_{\text{abs}}^2}$, in which $\tilde{k}_{\text{abs}}$ is the

complex propagation constant of the absorption material; and C_{mn}^{+} and C_{mn}^{-} are the constants. Considering the rigid boundary condition at the end $x = L_3 + h_1/2$, the pressure in the segment III, P_{tr}^{T2}, can be expressed as

$$P_{\mathrm{tr}}^{\mathrm{T2}}(x,y,z) = \sum_{m,n} \psi_{mn}(y,z) D_{mn} \times \left[e^{-iK_{mn}^{\mathrm{T2}}(x-(x_a+L_a))} + e^{iK_{mn}^{\mathrm{T2}}(x-(x_a+L_a)-2L_{III})} \right], \quad (12)$$

where L_{III} is the length of segment III of tube 2 and equals to $L_3 + h_1/2 - x_a - L_a$.

The responses in the three segments of tube 2 must satisfy the continuity of pressure and velocity over their interfaces, i.e.,

$$\begin{cases} P_{\mathrm{rad}}^{\mathrm{T2}} + P_{\mathrm{ref}}^{\mathrm{T2}} = P_{\mathrm{abs}}^{\mathrm{T2}} \\ \dfrac{1}{-i\omega\rho_0} \dfrac{\partial\left(P_{\mathrm{rad}}^{\mathrm{T2}} + P_{\mathrm{ref}}^{\mathrm{T2}}\right)}{\partial x} = \dfrac{1}{-i\omega\tilde{\rho}} \dfrac{\partial P_{\mathrm{abs}}^{\mathrm{T2}}}{\partial x}, \end{cases} \text{at } x = x_a, \quad (13)$$

and

$$\begin{cases} P_{\mathrm{abs}}^{\mathrm{T2}} = P_{\mathrm{tr}}^{\mathrm{T2}} \\ \dfrac{1}{-i\omega\tilde{\rho}} \dfrac{\partial P_{\mathrm{abs}}^{\mathrm{T2}}}{\partial x} = \dfrac{1}{-i\omega\rho_0} \dfrac{\partial P_{\mathrm{tr}}^{\mathrm{T2}}}{\partial x}, \end{cases} \quad \text{at } x = x_a + L_a, \quad (14)$$

where $\tilde{\rho}$ is the density of the absorption material. Other than above continuity conditions, the rigid boundary at $x = -L_2 - h_1/2$, the end of tube 2, must also be satisfied

$$\partial\left(P_{\mathrm{rad}}^{\mathrm{T2}} + P_{\mathrm{ref}}^{\mathrm{T2}}\right)/\partial x = 0. \quad (15)$$

Substituting Eqs. (9)–(12) into Eqs. (13)–(15), the unknown coefficients are solved as

$$B_{mn}^{+} = \frac{W_1 + W_2}{W_1 e^{iK_{mn}^{\mathrm{T2}}(2L_2+h_1)} - W_2}, \quad (16a)$$

$$B_{mn}^{-} = \frac{1 + e^{iK_{mn}^{\mathrm{T2}}(2L_2+h_1)}}{W_1 e^{iK_{mn}^{\mathrm{T2}}(2L_2+h_1)} - W_2} W_2, \quad (16b)$$

$$C_{mn}^{+} = \frac{e^{i\tilde{K}_{mn}^{\mathrm{T2}}L_a}}{2} \left[\left(1 + \frac{\tilde{\rho}K_{mn}^{\mathrm{T2}}}{\rho_0\tilde{K}_{mn}^{\mathrm{T2}}}\right) e^{i2K_{mn}^{\mathrm{T2}}L_{III}} + \left(1 - \frac{\tilde{\rho}K_{mn}^{\mathrm{T2}}}{\rho_0\tilde{K}_{mn}^{\mathrm{T2}}}\right) \right] \times \frac{\rho_0\omega Q_{mn}}{S^{\mathrm{T2}}K_{mn}^{\mathrm{T2}}} \frac{1 + e^{iK_{mn}^{\mathrm{T2}}(2L_2+h_1)}}{W_1 e^{iK_{mn}^{\mathrm{T2}}(2L_2+h_1)} - W_2}, \quad (16c)$$

$$C_{mn}^{-} = \frac{e^{-i\tilde{K}_{mn}^{\mathrm{T2}}L_a}}{2} \left[\left(1 - \frac{\tilde{\rho}K_{mn}^{\mathrm{T2}}}{\rho_0\tilde{K}_{mn}^{\mathrm{T2}}}\right) e^{i2K_{mn}^{\mathrm{T2}}L_{III}} + \left(1 + \frac{\tilde{\rho}K_{mn}^{\mathrm{T2}}}{\rho_0\tilde{K}_{mn}^{\mathrm{T2}}}\right) \right] \times \frac{\rho_0\omega Q_{mn}}{S^{\mathrm{T2}}K_{mn}^{\mathrm{T2}}} \frac{1 + e^{iK_{mn}^{\mathrm{T2}}(2L_2+h_1)}}{W_1 e^{iK_{mn}^{\mathrm{T2}}(2L_2+h_1)} - W_2}, \quad (16d)$$

and

$$D_{mn} = \frac{\rho_0\omega Q_{mn}}{S^{\mathrm{T2}}K_{mn}^{\mathrm{T2}}} \frac{\left[1 + e^{iK_{mn}^{\mathrm{T2}}(2L_2+h_1)}\right] e^{i2K_{mn}^{\mathrm{T2}}L_{III}}}{W_1 e^{iK_{mn}^{\mathrm{T2}}(2L_2+h_1)} - W_2}, \quad (16e)$$

where

$$W_1 = 2e^{i2K_{mn}^{\mathrm{T2}}L_{III}} \cosh\left(i\tilde{K}_{mn}^{\mathrm{T2}}L_a\right) + \left(\frac{\rho_0\tilde{K}_{mn}^{\mathrm{T2}}}{\tilde{\rho}K_{mn}^{\mathrm{T2}}} - \frac{\tilde{\rho}K_{mn}^{\mathrm{T2}}}{\rho_0\tilde{K}_{mn}^{\mathrm{T2}}}\right) e^{iK_{mn}^{\mathrm{T2}}x_a} \sinh\left(i\tilde{K}_{mn}^{\mathrm{T2}}L_a\right) + \left(\frac{\rho_0\tilde{K}_{mn}^{\mathrm{T2}}}{\tilde{\rho}K_{mn}^{\mathrm{T2}}} + \frac{\tilde{\rho}K_{mn}^{\mathrm{T2}}}{\rho_0\tilde{K}_{mn}^{\mathrm{T2}}}\right) e^{i2K_{mn}^{\mathrm{T2}}L_{III}} \sinh\left(i\tilde{K}_{mn}^{\mathrm{T2}}L_a\right), \quad (16f)$$

$$W_2 = 2e^{-iK_{mn}^{\mathrm{T2}}x_a} \cosh\left(i\tilde{K}_{mn}^{\mathrm{T2}}L_a\right) - \left(\frac{\rho_0\tilde{K}_{mn}^{\mathrm{T2}}}{\tilde{\rho}K_{mn}^{\mathrm{T2}}} + \frac{\tilde{\rho}K_{mn}^{\mathrm{T2}}}{\rho_0\tilde{K}_{mn}^{\mathrm{T2}}}\right) e^{-iK_{mn}^{\mathrm{T2}}x_a} \sinh\left(i\tilde{K}_{mn}^{\mathrm{T2}}L_a\right) - \left(\frac{\rho_0\tilde{K}_{mn}^{\mathrm{T2}}}{\tilde{\rho}K_{mn}^{\mathrm{T2}}} - \frac{\tilde{\rho}K_{mn}^{\mathrm{T2}}}{\rho_0\tilde{K}_{mn}^{\mathrm{T2}}}\right) e^{i2K_{mn}^{\mathrm{T2}}L_{III}} \sinh\left(i\tilde{K}_{mn}^{\mathrm{T2}}L_a\right), \quad (16g)$$

and

$$Q_{mn} = \frac{1}{\omega\rho_0} \sum_{q,r} K_{qr}^{\mathrm{T1}} \left[A_{qr}^{+} - A_{qr}^{-}\right] \sqrt{(2-\delta_{0q})(2-\delta_{0r})} \times \sqrt{(2-\delta_{0m})(2-\delta_{0n})}(-1)^{r+1} \times \frac{n/b_2 \sin(n\pi b_1/b_2)}{\pi\left[(r/b_1)^2 - (n/b_2)^2\right]} \frac{(-1)^q i2K_{mn}^{\mathrm{T2}} \sinh\left(iK_{mn}^{\mathrm{T2}}h_1/2\right)}{(2q\pi/h_1)^2 - \left(K_{mn}^{\mathrm{T2}}\right)^2}.$$

Substituting Eqs. (16a) and (16b) into Eqs. (9) and (10), $P_{\mathrm{rad}}^{\mathrm{T2}}$ and $P_{\mathrm{ref}}^{\mathrm{T2}}$ can be expressed in terms of A_{qr}^{+} and A_{qr}^{-} as

$$P_{\mathrm{rad}}^{\mathrm{T2}}(x,y,z) = i \sum_{q,r} K_{qr}^{\mathrm{T1}} \left[A_{qr}^{+} - A_{qr}^{-}\right] \sqrt{(2-\delta_{0q})(2-\delta_{0r})} \times \sum_{m,n} \frac{\sqrt{(2-\delta_{0m})(2-\delta_{0n})}\psi_{mn}(y,z)}{S^{\mathrm{T2}}\left[(2q\pi/h_1)^2 - \left(K_{mn}^{\mathrm{T2}}\right)^2\right]} \times \frac{(-1)^{r+1} n/b_2 \sin(n\pi b_1/b_2)}{\pi\left[(r/b_1)^2 - (n/b_2)^2\right]} G_{mn}, \quad (17)$$

where

$$G_{mn} = \begin{cases} \cos\frac{2q\pi x}{h_1} - (-1)^q e^{-iK_{mn}^{\mathrm{T2}}h_1/2} \cosh(iK_{mn}^{\mathrm{T2}}x), & -\frac{h_1}{2} \le x \le \frac{h_1}{2} \\ (-1)^q \sinh\left(iK_{mn}^{\mathrm{T2}}h_1/2\right) e^{-iK_{mn}^{\mathrm{T2}}x}, & x > \frac{h_1}{2} \\ (-1)^q \sinh\left(iK_{mn}^{\mathrm{T2}}h_1/2\right) e^{-iK_{mn}^{\mathrm{T2}}x}, & x < -\frac{h_1}{2} \end{cases},$$

and

$$P_{\mathrm{ref}}^{\mathrm{T2}}(x,y,z) = i \sum_{q,r} K_{qr}^{\mathrm{T1}} \left(A_{qr}^{+} - A_{qr}^{-}\right) \sqrt{(2-\delta_{0q})(2-\delta_{0r})} \times \sum_{m,n} \frac{\sqrt{(2-\delta_{0m})(2-\delta_{0n})}\psi_{mn}(y,z)}{S^{\mathrm{T2}}\left[(2q\pi/h_1)^2 - \left(K_{mn}^{\mathrm{T2}}\right)^2\right]} \times \frac{(-1)^{r+1} n/b_2 \sin(n\pi b_1/b_2)}{\pi\left[(r/b_1)^2 - (n/b_2)^2\right]} \times \frac{(-1)^q \sinh\left(iK_{mn}^{\mathrm{T2}}h_1/2\right)}{W_1 e^{iK_{mn}^{\mathrm{T2}}(2L_2+h_1)} - W_2} \times \left\{ (W_1 + W_2) e^{-iK_{mn}^{\mathrm{T2}}x} + W_2 \left[1 + e^{iK_{mn}^{\mathrm{T2}}(2L_2+h_1)}\right] e^{iK_{mn}^{\mathrm{T2}}x} \right\}. \quad (18)$$

At the interface of tubes 1 and 2, the boundary condition of pressure is

$$p^{T1}|_{y=0} = P^{T2}_{rad} + P^{T2}_{ref}|_{y=0}, |x| \le \frac{h_1}{2}, |z| \le \frac{b_1}{2}. \tag{19}$$

Multiplying both sides of Eq. (19) by $\phi_{\mu\nu}(x, z)$ and integrating them over the cross-sectional area of tube 1 yield

$$\iint_{S^{T1}} P^{T1}|_{y=0}\phi_{\mu\nu}(x,z)dxdz = \iint_{S^{T1}} \left[P^{T2}_{rad} + P^{T2}_{ref}|_{y=0}\right]\phi_{\mu\nu}(x,z)dxdz. \tag{20}$$

Substituting Eqs. (2), (17), and (18) into Eq. (20) gives

$$\begin{aligned} A^+_{\mu\nu} + A^-_{\mu\nu} = {} & \frac{i}{S^{T1}S^{T2}} \sum_{q,r} K^{T1}_{qr}\left[A^+_{qr} - A^-_{qr}\right]\sqrt{(2-\delta_{0q})(2-\delta_{0r})} \\ & \times \sqrt{(2-\delta_{0\mu})(2-\delta_{0\nu})} \sum_{m,n} \frac{(2-\delta_{0m})(2-\delta_{0n})}{(2q\pi/h_1)^2 - (K^{T2}_{mn})^2} \\ & \times \frac{(-1)^{r+\nu}(n/\pi b_2)^2 \sin^2(n\pi b_1/b_2)}{\left[(r/b_1)^2 - (n/b_2)^2\right]\left[(\nu/b_1)^2 - (n/b_2)^2\right]} \\ & \times \left\{ \beta h_1 + (-1)^{q+\mu} \frac{i2K^{T2}_{mn}\sinh^2(iK^{T2}_{mn}h_1/2)}{(2\mu\pi/h_1)^2 - (K^{T2}_{mn})^2} \right. \\ & \times \left[\frac{W_1 + W_2\left(2 + e^{iK^{T2}_{mn}(2L_2+h_1)}\right)}{W_1 e^{iK^{T2}_{mn}(2L_2+h_1)} - W_2} \right. \\ & \left. \left. - \frac{e^{-iK^{T2}_{mn}h_1/2}}{\sinh(iK^{T2}_{mn}h_1/2)} \right] \right\}, \end{aligned} \tag{21}$$

where

$$\beta = \begin{cases} 1, & q = \mu = 0 \\ 1/2, & q = \mu \neq 0 \\ 0, & q \neq \mu \end{cases}$$

Combining Eqs. (6) and (7) with Eq. (21), the modal response A^+ and A^- can thus be obtained. If the absorption materials are removed from tube 2, the terms W_1 and W_2 in Eqs. (16f) and (16g) become $2e^{iK^{T2}_{mn}(2L_3+h_1-x_a-L_a)}$ and $2e^{-iK^{T2}_{mn}(x_a+L_a)}$, respectively. Substituting W_1 and W_2 into Eq. (21), the first item in the square brackets on the right hand side of this equation changes to $[e^{iK^{T2}_{mn}(2L_2+h_1)} + e^{iK^{T2}_{mn}(2L_3+h_1)} + 2]/[e^{i2K^{T2}_{mn}(L_2+L_3+h_1)} - 1]$. Using this modified equation, the pressure field inside an empty TAR can be consequently solved.

Based on the obtained pressure field, the input acoustic impedance of the TAR is computed as

$$Z_{in} = \frac{\frac{1}{S^{T1}}\iint_{S^{T1}} P^{T1}(x, -L^{T1}_{eff}, z)dxdz}{S^{T1}U_S}. \tag{22}$$

Substituting Eq. (2) into Eq. (22), Z_{in} is simplified as

$$Z_{in} = \left(A^+_0 e^{iK^{T1}_0 L^{T1}_{eff}} + A^-_0 e^{-iK^{T1}_0 L^{T1}_{eff}}\right)/S^{T1}U_S. \tag{23}$$

At resonances, the imaginary part of Z_{in} is zero. Consequently, the natural frequencies f_r of the TAR can be obtained from Eq. (23) after setting the imaginary part of Z_{in} to zero. Benefits of the long TAR is in that its high-order resonances are very low compared with a conventional HR, and therefore, apart from the fundamental resonance, these high-order resonances have potential to be utilized simultaneously in noise control applications.

III. SIMULATIONS AND EXPERIMENTAL VALIDATIONS

The resonance frequencies of TARs were numerically predicted and experimentally validated. The experimental set-up is shown in Fig. 2(a). The TAR was excited by a loudspeaker which was driven by a white noise signal from Bruel & Kjaer PULSE system. Two Bruel & Kjaer type 4189 ½ inch microphones were used to measure the frequency response functions (FRFs). One microphone was fixed outside the TAR and near its orifice to measure the external excitation and another was inserted into tube 2 at its end at $x = L_3 + h_1/2$ to measure the sound pressure inside the resonator. The peaks of the FRF indicated resonances. A tunable TAR was fabricated with two square tubes as shown in Fig. 2(b). The length of tube 1 was 30.1 mm with a cross-sectional dimensions of 20.0×20.0 mm^2. The cross-section dimensions of tube 2 were 40.3×40.2 mm^2 and L_2 was 30.0 mm. L_3 can be varied by adjusting the total length of tube 2 and consequently the resonance frequency of the TAR can be tuned. Given ambient temperature of 20°C, the sound speed was determined as 344.5 m/s. The air density ρ_0 was 1.205 kg/m^3. The specific heat ratio of the air was 1.402. The thermal conductivity of air was 0.0266 W/m K. The specific heat at constant pressure of the air was 1005 J/kg K. The coefficient of shear viscosity was 1.88e-5 Pa s.

In simulations, the vibration amplitude of the piston was set to 1, namely $U_S = 1$ in Eq. (5). The number of truncated modes was determined by a convergence study. Finally, four cross-sectional modes for tube 1 and 36 cross-sectional modes for tube 2 were used. It should be noted that since the number of truncated modes is small, the transfer matrix was solved directly in this work. When a large number of modes are required, the method of the local impedance matrix[21] should be adopted to avoid singularity of matrix.

A. Experimental validation

1. Without absorption materials

The model validation is focused on the first two natural frequencies of the TAR. In the study of the first natural frequency, the value of L_3 was varied from 50 to 550 mm in both simulations and experiments, and in the study of the second natural frequency, L_3 was varied from 100 to 550 mm. The response inside the TAR was calculated by the combination of Eqs. (6), (7), and (21). Using the computed responses, the input impedance was calculated by Eq. (23). The predicted two natural frequencies are plotted in Fig. 3. It is seen that the two natural frequencies were very sensitive

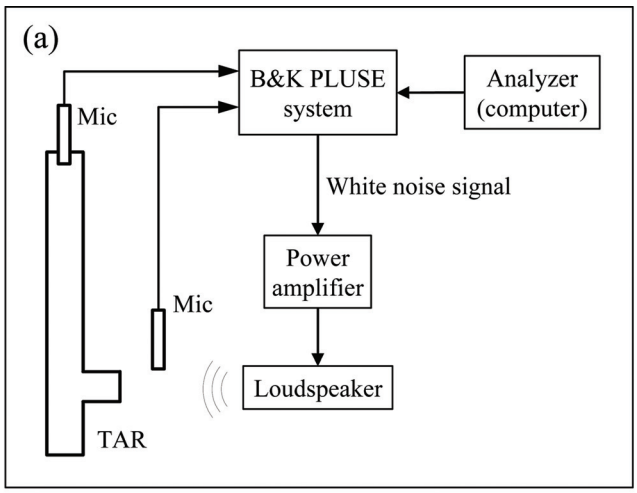

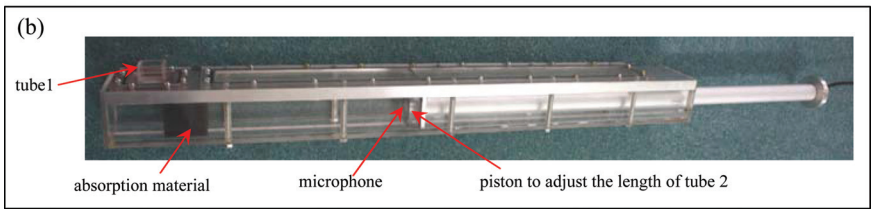

FIG. 2. (Color online) (a) Experimental system and (b) tunable TAR.

to L_3. As L_3 increased, the fundamental frequency decreased gradually from 401.2 to 117.9 Hz. Owing to the long profile of tube 2, the second natural frequency reached the value as low as 360.1 Hz when L_3 was 550 mm. For a conventional HR using above tube 1 as its neck and having a body with the same volume as tube 2 ($L_3 = 550$ mm), it is impossible to obtain such a low second natural frequency. For example, if the body of the HR is cubic, its second natural frequency predicted by the boundary element method (BEM) was around 1805 Hz, which is much larger than 360.1 Hz.

Experiments were carried out at ten values of L_3 which were equally spaced. The obtained natural frequencies in each case are also plotted in Fig. 3. The comparisons between simulations and experiments show that for the fundamental frequency, the maximum prediction error was about 0.70%, occurring at $L_3 = 250$ mm, and for the second natural frequency, the errors of predictions were limited within 0.31%. Experimental results and the predictions are also listed in Table I for reference. Generally speaking, for both the fundamental frequency and the second natural frequency, predictions by the current model agreed very well with experiments.

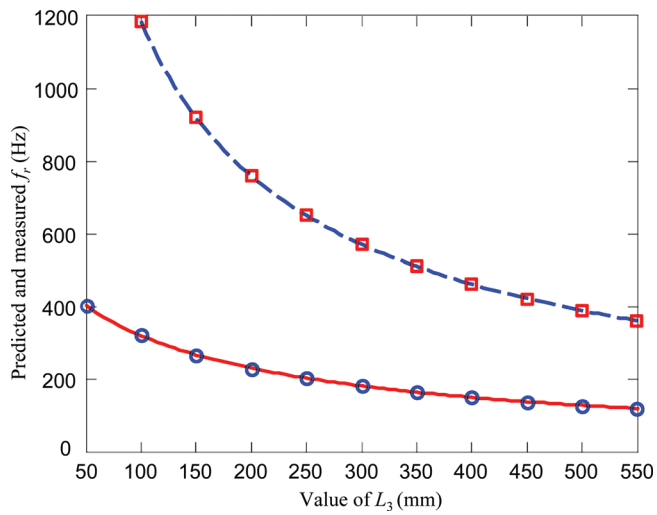

FIG. 3. (Color online) Comparison between predicted and measured resonance frequencies with the variation of L_3: — predicted fundamental frequency from current model; ○ measured fundamental frequency; — — predicted second natural frequency from current model; and □ measured second natural frequency.

2. With absorption materials

In this part of validation, sound absorption materials were inserted into tube 2. Since the absorption performance of materials depends on the air particle speed, the materials cannot be installed at an arbitrary location inside tube 2. The experience from HR study suggests that a good location for installing the absorption materials is at the internal end of the neck but not in the body since the particle velocity inside the body of HR is very small. The long profile of TARs, however, may results in a velocity field different from conventional HRs. To properly locate the absorption materials, it is necessary to understand the velocity distribution in tube 2. Taking the TAR with $L_3 = 400$ mm as an example, the velocity amplitude was computed at the fundamental resonance frequency and is shown in Fig. 4. Figure 4(a) depicts the velocity contour at the surface $z = 0$. It can be observed that in tube 2, the vibration of air particles was strong in its longer segment (L_3) and was very weak in its shorter segment (L_2). To show this point more clearly, the velocity amplitude along the axis of tube 2 is plotted in Fig. 4(b). It is seen that the velocity reached its maximum at $x = 8$ mm. On the left hand side of this maximum, the velocity attenuated rapidly; while on the other side, the velocity kept at a high level in a relatively large range of x. The velocity distribution in Fig. 4

TABLE I. Measured and predicted natural frequencies without absorption materials.

	Measured f_r (Hz)		Predicted fr (Hz)		Deviation of prediction (Hz)		Prediction error (%)	
$L3$ (mm)	Fundamental	Second	Fundamental	Second	Fundamental	Second	Fundamental	Second
50	401.5	—	401.2	—	−0.3	—	0.07	—
100	319.3	1182.5	318.7	1183.2	−0.6	0.7	0.19	0.06
150	266.5	919.5	266.2	918.7	−0.3	−0.8	0.11	0.09
200	228.0	758.8	229.3	758.8	1.3	0.0	0.57	0.00
250	200.3	650.5	201.7	650.1	1.4	−0.4	0.70	0.06
300	179.3	571.0	180.1	570.6	0.8	−0.4	0.45	0.07
350	162.0	509.8	162.8	509.5	0.8	−0.3	0.49	0.06
400	147.8	459.8	148.6	461.0	0.8	1.2	0.54	0.26
450	136.3	421.0	136.7	421.3	0.4	0.3	0.29	0.07
500	126.0	387.5	126.6	388.2	0.6	0.7	0.48	0.18
550	117.3	359.0	117.9	360.1	0.6	1.1	0.51	0.31

suggests that the effect of the tube 2 was dominated by its longer segment under the first resonance condition. It should be a typical feature for TARs since tube 1 is usually installed near one end of tube 2. Therefore, the absorption material was installed inside the above longer segment (L_3) close to the maximum velocity region at $x_a = h_1/2$ (10 mm). It is pertinent to note that the contour in Fig. 4(a) illustrates the nonplane wave propagation at locations not far from the junction of two tubes, which suggests the importance of the consideration of high-order modes.

Two different fully reticulated polyurethane foams were used as absorption materials in experiments. Their characteristic impedance and wave-number were measured by using an impedance tube.[22] For the two foams, the one having lower characteristic impedance was named as foam 1 and another having higher characteristic impedance was denoted by foam 2. The length of foams 1 and 2 (L_a) was 40.8 and 39.9 mm, respectively. After assigning the properties of the foams by the measured data, the FRFs were calculated between the averaged pressure at the end $L_3 + h_1/2$ of tube 2 and that over the orifice of the TAR. The predicted and measured FRFs with and without absorption materials for an arbitrary case of $L_3 = 400$ mm are compared in Fig. 5. It can be seen that the predictions agree satisfactorily with experimental results. The empty TAR (see Table I) led to a fundamental frequency of 148.6 Hz in simulations. After the insertion of two foams, this frequency moved to 144.3 and 138.9 Hz, respectively, both of which are close to the experimental results, i.e., 145.3 and 141.3 Hz. As expected, the absorption foams reduced the natural frequency since they enhanced the damping effect inside the TAR. This effect can be quantitatively described by the Q-factors obtained from the FRF curves, which are listed in Table II. The measured Q-factor for the empty TAR was 29.56, while after inserting the foams the measured Q-factor was reduced to 9.56 and 3.73, respectively. The similar Q-factors of the TAR with foams were also predicted by the current model which gave 9.34 and 3.57, respectively.

Using the foam 2 and varying L_3 from 250 to 550 mm with a step of 50 mm, the predictions from the current model were further compared with experiments. The length of this foam remained the same as before. The obtained results are tabulated in Table III, which shows that the errors of the predicted results by the current model were generally lower than 2.2%. The predictions are in good agreement with the experimental results in all configurations.

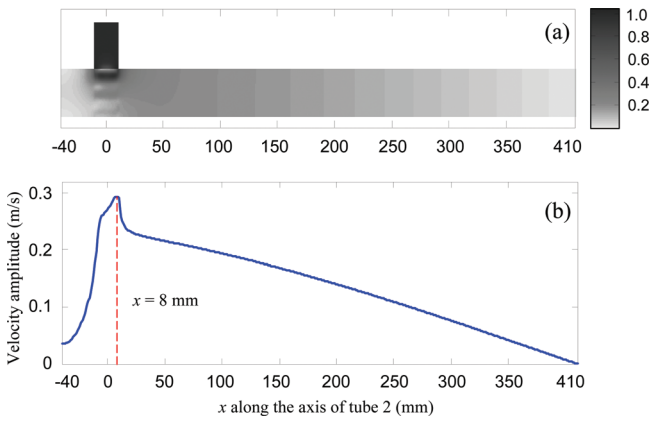

FIG. 4. (Color online) Velocity distribution.

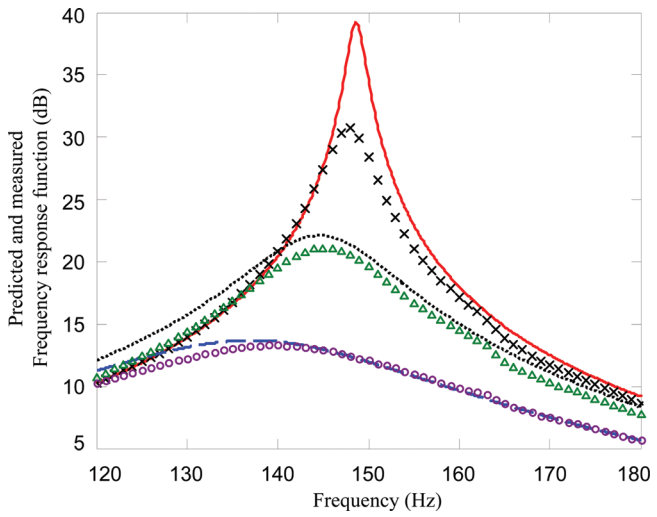

FIG. 5. (Color online) Measured and predicted FRFs: — prediction for empty TAR; × measurement for empty TAR; ··· prediction for TAR with foam 1; Δ measurement for TAR with foam 1; — — prediction for TAR with foam 2; and o measurement for TAR with foam 2.

TABLE II. Measured and predicted Q-factors.

Foam in TAR	Predicted Q-factor	Measured Q-factor
Foam 1	9.34	9.56
Foam 2	3.57	3.73

It is therefore concluded that the current model is accurate and reliable enough to guide the TAR design no matter whether absorption materials are presented or not.

B. Analyses

1. Comparisons with the 1-D model and the FEM model

It is relevant to compare the current 3-D model with the FEM model and the 1-D model. The equation to compute the natural frequencies of the TAR obtained by 1-D model is[7]

$$1 - \frac{S^{T2}}{S^{T1}}\tan[k(L_1 + \Delta L_1)]\{\tan[k(L_2 + \Delta L_2)] + \tan[k(L_3 + \Delta L_3)]\} = 0, \quad (24)$$

where ΔL_1, ΔL_2, and ΔL_3 are the end corrections of the three branches, respectively. According to the hybrid Rayleigh's end corrections, ΔL_1 only counts the external end correction of the TAR, and ΔL_2 equal to ΔL_3 is 1.5 times ΔL_1. Since these end corrections were developed for the circular tubes, to apply them for the square tubes in the current work, the tube 1 was replaced by an equivalent circular tube with the same cross-sectional area in simulations. ΔL_1 was consequently calculated by $8r_1/3\pi$, where r_1 is the radius of the equivalent circular tube and computed by $\sqrt{S^{T1}/\pi}$. This equivalent method was applied to rectangular orifice in previous works.[7,9] For the FEM model, the length of tube 1 was the sum of its physical length and the external end correction which is the same as that used in the current model. A uniform velocity distribution was exerted over the orifice surface.

a. Prediction accuracy. To compare the accuracy of the current model with other existing models, the experimental results in Table I were used again to benchmark the predictions. In numerical simulations, the dimensions of the TAR and the variation of L_3 were the same as those used in experiments in Sec. III A 1. The predicted two natural frequencies by the 1-D and FEM models are listed in Table IV. The deviations of these predictions from the measured values are compared in Fig. 6. It is observed from Fig. 6(a) that for the fundamental frequency, the accuracy of the FEM model is near that of the current model. The 1-D model produced deviations up to 4.5 Hz (minus) that is much higher than 1.4 Hz, which is the maximum deviation of the current model. The overall deviation level of the current model was much lower than that of the 1-D model. Better performance of the current model can be also expected on the prediction of high-order resonances, such as the second natural frequency shown in Fig. 6(b). It can be seen that the deviations to the measured results obtained by the current model and the FEM model were similar for most of the tested L_3, while the deviations to the measured results obtained by the 1-D model were as large as 15 Hz. The absolute deviations of the current model to the measured results were smaller than 1.2 Hz, which is much better than that of the 1-D model.

Note that the deviation tendency shown in Fig. 6 also suggests the 1-D model with the hybrid Rayleigh's end corrections performed well for TARs with a long tube 2 ($L_3 \geq 400$ mm). This is consistent with the simplification requirement for 1-D duct, i.e., the ratio of L_3 to h_2 (40.3 mm and larger than b_2) better to be larger than 10.[9–11]

b. Effects of TAR dimensions. It is observed from Eq. (24) that the prediction on the natural frequencies by 1-D model only depends on the cross-sectional areas and lengths of tubes. Actually, if the ratio of the cross-sectional width to height of the tubes is varied, it will greatly affect the natural frequencies. However, the effect of that cross-sectional ratio variation was not modeled in any 1-D models. To clarify this aspect, simulations were carried out for different cross-section aspect ratios for tube 2. In simulations, L_3 was fixed at 300 mm, the cross-sectional area of tube 2 was fixed at 1620.06 mm^2, the ratio of h_2 to b_2 was varied from 0.3 to 3, while other geometric dimensions of the TAR remained the same as those used in experiments. It should be noted that during the variation of the above ratios, the maximum transverse dimension was 73.5 mm and the ratio of L_3 to this value was 4. This ratio is larger than 3, the minimum requirement for 1-D simplification,[10] and hence the 1-D model is still applicable for such an extreme geometry. Since the current model has been validated by experiments, the 1-D model and the FEM model were directly compared with the current model. The fundamental frequencies predicted by the three models are plotted in Fig. 7. The figure shows that the 1-D model gave a constant fundamental frequency when h_2/b_2 changed. The predictions from the current model

TABLE III. Measured and predicted fundamental frequency after inserting absorption material.

$L3$ (mm)	Measured fr (Hz)	Predicted fr (Hz)	Absolute deviation of predictions (Hz)	Prediction error (%)
250	191.3	191	0.3	0.16
300	171	170	1.0	0.58
350	154.3	153	1.3	0.84
400	141.3	138.9	2.4	1.70
450	128.8	126.8	2.0	1.55
500	118.8	116.2	2.6	2.19
550	108.5	106.9	1.6	1.47

TABLE IV. Predicted two natural frequencies by 1-D model and FEM model and absolute deviations of these predictions from experimental results.

	1-D model				FEM model in sysnoise			
	f_r (Hz)		Deviation (Hz)		f_r (Hz)		Deviation (Hz)	
L3 (mm)	Fundamental	Second	Fundamental	Second	Fundamental	Second	Fundamental	Second
50	397	—	−4.5	—	402.7	—	1.2	—
100	319.2	1119.9	−0.1	−62.6	319.8	1188.9	0.5	6.4
150	268	883.7	1.5	−35.8	267.1	921.2	0.6	1.7
200	231.3	737.9	3.3	−20.9	230	760.3	2.0	1.5
250	203.6	637.1	3.3	−13.4	202.2	651.1	1.9	0.6
300	181.9	562.4	2.6	−8.6	180.6	571.4	1.3	0.4
350	164.5	504.4	2.5	−5.4	163.2	510.2	1.2	0.4
400	150.1	457.8	2.3	−2.0	148.9	461.6	1.1	1.8
450	138	419.4	1.7	−1.6	137	421.8	0.7	0.8
500	127.7	387.2	1.7	−0.3	126.8	388.7	0.8	1.2
550	118.9	359.6	1.6	0.6	118.1	360.5	0.8	1.5

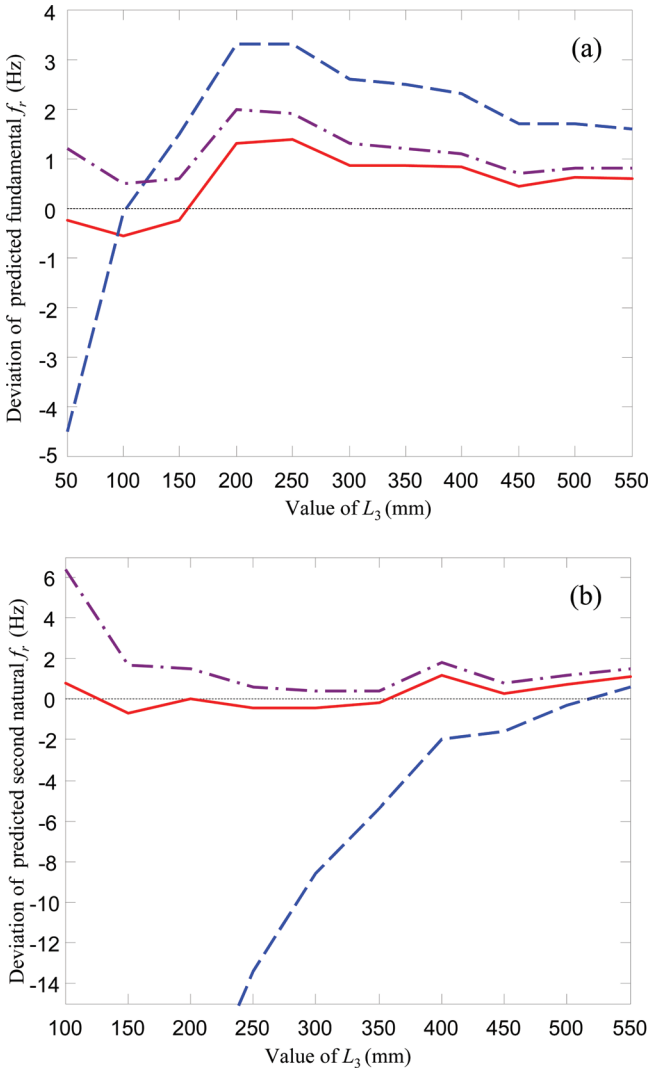

FIG. 6. (Color online) Absolute deviation of predicted natural frequencies from experimental results. (a) Fundamental frequency: — current model; — —1-D model; — • — FEM model; (b) Second natural frequency: — current model; — — 1-D model; — • — FEM model.

and FEM model, however, showed a clear dependence of the resonance frequency on h_2/b_2 with very similar tendency. A maximum 3.9 Hz variation on the fundamental frequency was obtained from the current model. The 1-D model seems to better apply to rectangular cross-sections when h_2/b_2 is near unit or circular cross-sections.

Apart from the requirement on the cross-sectional dimensions of tubes, the limitation on the length of tube 1 is also strict, especially in case where the space is a concern. However, a short tube 1 probably reduces the accuracy of the 1-D model in which the tube 1 is assumed to be a 1-D pipe. This surmise can be ascertained from Fig. 8, in which the predicted fundamental frequencies from three models with respect to the length of tube 1 are compared. In simulations, L_3 was fixed at 300 mm and the length of tube 1 was varied from 5 to 50 mm. It can be seen that the predictions of the current model and the FEM model were almost in

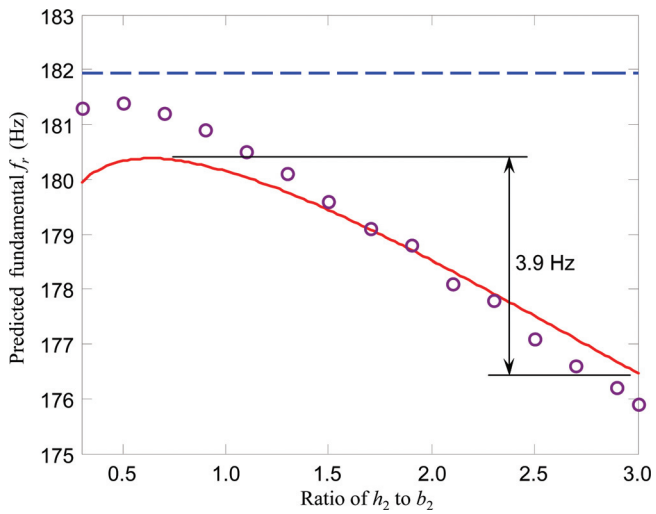

FIG. 7. (Color online) Predicted fundamental frequency by different models with the different ratios of h_2 to b_2: — current model; — — 1-D model; and o FEM model.

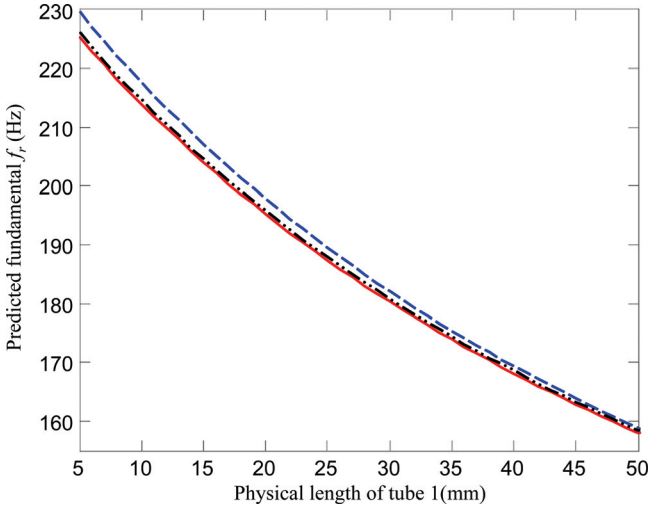

FIG. 8. (Color online) Predicted fundamental frequency with the different length of tube 1: — current model; — — 1-D model; and — • • — FEM model.

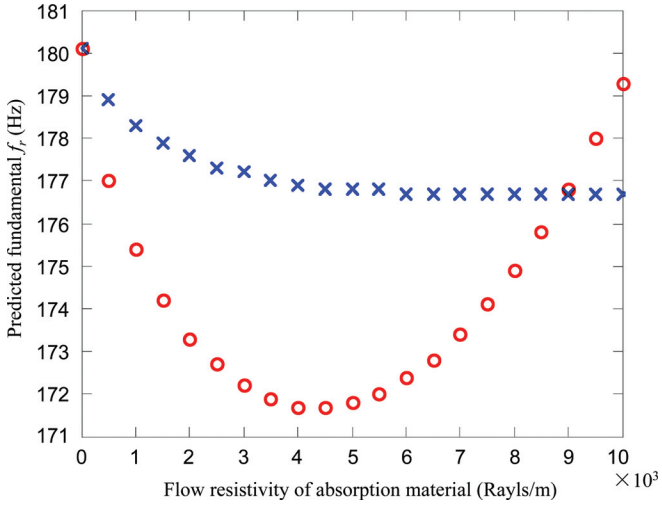

FIG. 9. (Color online) Predicted fundamental frequency with the variation of the flow resistivity. ○ absorption material at $x = h_1/2$; × absorption material at $x = L_3 + h_1/2 - L_a$.

perfect agreement, with a maximum difference of 1 Hz or so. In contrast, the differences between the predictions by the 1-D model and the 3-D model increased up to 4.4 Hz with the decrease of the length of tube 1. No doubt, the 1-D model better approaches the real resonance for a long tube 1.

2. Effect of absorption materials

As it is observed from the FRF curves in Fig. 5, the performance of the TAR was influenced by the properties of the absorption materials, i.e., the characteristic impedance and wave-number. To fully understand the effects of these parameters, simulations were also conducted by using glass fibers with variable flow resistivities, from which the characteristic impedance and wave-number were calculated.[23] In simulations, L_a was fixed to 40 mm and the flow resistive was varied from 500 to 10 000 Rayls/m. The absorption materials were fixed at two different locations: the opening and close end of the longer segment of tube 2 (L_3), i.e., at $x = h_1/2$ and $x = L_3 + h_1/2 - L_a$, respectively. The fundamental frequency was predicted and is shown in Fig. 9. It is found that when the absorption material was fixed at the close end ($x = L_3 + h_1/2 - L_a$), as the flow resistivity increased, the fundamental frequency only varied slightly and slowly converged to a constant value. A plausible explanation for it is that the particle velocity is very small at this location as shown in Fig. 4(a) and hence the damping effect is weak even for a large flow resistivity. In contrast, when the material was fixed at the opening ($x = h_1/2$) where the particle velocity was large, the fundamental frequency became sensitive to the flow resistivity and underwent more obvious variations. The increase in the flow resistivity first induced a decrease of the fundamental frequency due to an enhancement of the damping inside the TAR. After reaching the lowest value, the fundamental frequency reversed to rise quickly with the further increase of the flow resistivity. As expected, in such cases an excessive flow resistivity weakens the communication or connectivity between the two sections (I and III) of tube 2 separated by the absorption materials. This equivalently shortens the effective length of tube 2 and results in the increase of the fundamental frequency. One can surmise that when the flow resistivity tends to infinite, it will completely neutralize the effect of the sections II and III of tube 2 shown in Fig. 1, leading to a significant increase in the fundamental frequency. It is noted that the variation tendency of the fundamental frequency for the installation case with $x = h_1/2$ is quite different from that of conventional HRs[12] which is more similar to the case where the sound absorption materials are installed at the end of the tube.

Resonances of TARs are also affected by the thickness of the absorption materials as illustrated in Fig. 10. Foam 2 was employed again in this simulation and its L_a was varied from 0 to 100 mm, while L_3 was kept to 300 mm as it was used in the above section. It was found that with the increase of the thickness, the fundamental frequency decreased, attributing to the effect of damping increase inside the TAR.

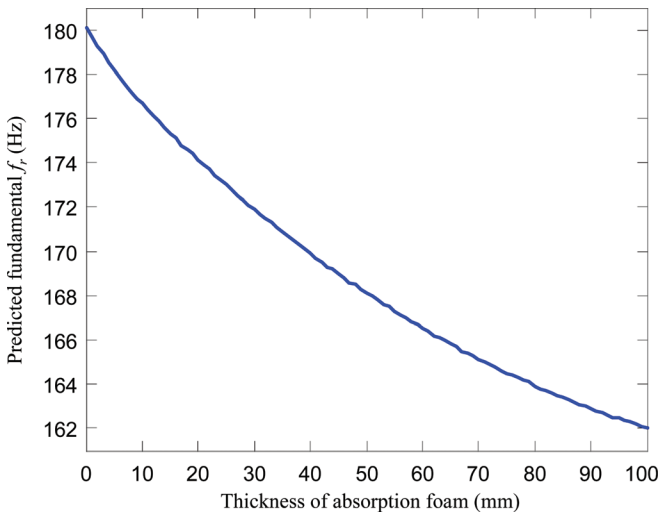

FIG. 10. (Color online) Predicted fundamental frequency with the variation of the thickness of foam.

IV. CONCLUSIONS

A 3-D model is developed and experimentally validated to characterize the TAR having inserted absorption materials. Compared with the existing 1-D models, the 3-D model is much more in that it can accommodate various geometrical parameters of TAR as well as the presence of the sound absorption materials. It is demonstrated that the proposed 3-D model can predict the resonance frequencies of TARs more accurately and eventually can meet the requirement for resonator array design in terms of accuracy. More specifically, typical errors of the predictions by the 3-D model from measured data are caped within 0.70% and 0.31% for the first two natural frequencies, respectively. Meanwhile, existing 1-D model with empirical end corrections is found to perform well only for TARs consisting of long tubes. It is also found that the resonance frequencies are sensitive to the location of the absorption materials inside the long closed-end tube. A moderate increase in either flow resistivity or length of the absorption materials results in a reduction of the resonance frequencies due to the enhanced damping effect inside the TAR. An excessive increase in the flow resistivity, however, can induce a significant increase of the resonance frequencies, which is different from the conventional HRs.

ACKNOWLEDGMENT

The authors wish to acknowledge the support from Innovation and Technology Fund from Hong Kong, China (Project No. ZP1P). Technical assistant from Wai Har in carrying out experiments is also acknowledged.

[1]S. A. Lane, R. E. Richard, and S. J. Kennedy, "Fairing noise control using tube-shaped resonators," J. Spacecr. Rockets **42**, 640–646 (2005).

[2]D. Li and J. S. Vipperman, "Noise control of mock-scale chambercore payload fairing using integrated acoustic resonators," J. Spacecr. Rockets **43**, 877–882 (2006).

[3]D. Li, L. Cheng, G. Yu, and J. S. Vipperman, "Noise control in enclosures: Modeling and experiments with T-shaped acoustic resonators," J. Acoust. Soc. Am. **122**, 2615–2625 (2007).

[4]G. Yu and L. Cheng, "Location optimization of a long T-shaped acoustic resonator array in noise control of enclosures," J. Sound Vib. **328**, 42–56 (2009).

[5]Deyu Li, Xiao-Hong Zhang, Li Cheng, and Ganghua Yu, "Effectiveness of T-shaped acoustic resonators in low-frequency sound transmission control of a finite double-panel partition," J. Sound Vib. **329**, 4740–4755 (2010).

[6]P. Merkli, "Acoustic resonance frequencies for a T-tube," Z. Angew. Math. Phys. **29**, 486–498 (1978).

[7]D. Li and J. S. Vipperman, "On the design of long T-shaped acoustic resonators," J. Acoust. Soc. Am. **116**, 2785–2792 (2004).

[8]V. Dubos, J. Kergomard, A. Khettabi, J.- P. Dalmont, D. H. Keefe, and C. J. Nederveen, "Theory of sound propagation in a duct with a branched tube using modal decomposition," Acust. Acta Acust. **85**, 153–169 (1999).

[9]R. L. Panton and J. M. Miller, "Resonant frequencies of cylindrical Helmholtz resonators," J. Acoust. Soc. Am. **57**, 1533–1535 (1975).

[10]R. C. Chanaud, "Effects of geometry on the resonance frequency of Helmholtz resonators," J. Sound Vib. **178**, 337–348 (1994).

[11]A. Selamet, P. M. Radavich, N. S. Dickey, and J. M. Novak, "Circular concentric Helmholtz resonators," J. Acoust. Soc. Am. **101**, 41–51 (1997).

[12]A. Selamet and Z. L. Ji, "Circular asymmetric Helmholtz resonators," J. Acoust. Soc. Am. **107**, 2360–2369 (2000).

[13]A. Selamet, M. B. Xu, I. J. Lee, and N. T. Huff, "Helmholtz resonator lined with absorbing material," J. Acoust. Soc. Am. **117**, 725–733 (2005).

[14]G. H. Yu, D. Li, and L. Cheng, "Effect of internal resistance of a Helmholtz resonator on acoustic energy reduction in enclosures," J. Acoust. Soc. Am. **124**, 3534–3543 (2008).

[15]F. J. Fahy, *Sound and Structural Vibration: Radiation, Transmission and Response* (Academic Press, London, 2007), Chap. 7, p. 419.

[16]A. D. Pierce, *Acoustics: An Introduction to its Physical Principles and Applications* (Acoustic Society of America, New York, 1989), Chap. 10, p. 534.

[17]U. Ingard, *Notes on Acoustics* (Jones & Bartlett Publishers, Massachusetts, 2008), Chap. A, pp. 394–396.

[18]P. M. Morse and K. U. Ingard, *Theoretical Acoustics* (McGraw-Hill, New York, 1968), Chap. 7, pp. 392–394.

[19]P. E. Doak, "Excitation, transmission and radiation of sound from source distributions in hard-walled ducts of finite length. I—The effects of duct cross-section geometry and source distribution space-time pattern," J. Sound Vib. **31**, 1–72 (1973).

[20]L. Huang, "Modal analysis of a drumlike silencer," J. Acoust. Soc. Am. **112**, 2014–2025 (2002).

[21]V. Pagneux, N. Amir, and J. Kergomard, "A study of wave propagation in varying cross-section waveguides by modal decomposition. Part I. Theory and validation," J. Acoust. Soc. Am. **100**, 2034–2048 (1996).

[22]H. Utsuno, T. Tanaka, T. Fujikawa, and A. F. Seybert, "Transfer function method for measuring characteristic impedance and propagation constant of porous materials," J. Acoust. Soc. Am. **86**, 637–643 (1989).

[23]M. E. Delany and E. N. Bazley, "Acoustical properties of fibrous absorbent material," Appl. Acoust. **3**, 105–116 (1970).